**Structural Engineering and Mechanics**, *Vol. 62, No. 4 (2017) 497-506*
DOI: https://doi.org/10.12989/sem.2017.62.4.497


# Response of self-centering braced frame to near-field pulse-like ground motions

Navid Rahgozar[1a], Abdolreza S. Moghadam[*2] and Armin Aziminejad[1b]

[1]*Department of Structural Engineering, Science and Research Branch, Islamic Azad University, Tehran, Iran*
[2]*Department of Civil Engineering, International Institute of Earthquake Engineering and Seismology (IIEES), Tehran, Iran*

*(Received August 7, 2015, Revised December 2, 2016, Accepted February 10, 2017)*

**Abstract.** A low damage self-centering braced frame equipped with post-tensioning strands is capable of directing damage to replaceable butterfly-shaped fuses. This paper investigates the seismic performance of rocking braced frame under near-field pulse-like ground motions compared to far-field records. A non-linear time history analysis is performed for twelve self-centering archetypes. A sensitivity analysis is carried out to examine the influences of ground motion types and modeling parameters. Findings represent the proper efficiency of the self-centering system under both far-field and near-field pulse-like ground motions.

**Keywords:** self-centering braced frame archetype; far-field and near-field pulse-like ground motions; nonlinear time history analysis; engineering demand parameters

## 1. Introduction

Current seismic design codes (e.g., ASCE 2010, IBC 2006) provide the efficient design methods to control the structural damage of conventional buildings (Ye and Otani 1999). However, damage reduction of conventional buildings under an earthquake has been growing interest among researchers. Recently, various types of self-centering systems as the modern low-damage systems, whose basic concept was first introduced by Housner (1963) have been developed. Steel self-centering frames (Iwashita *et al.* 2002), rocking wall-frame structures (Ajrab *et al.* 2002, Grigorian and Grigorian 2015), rocking timber systems (Francesco *et al.* 2015), and confined masonry rocking walls (Toranzo *et al*. 2009) are examples of such low-damage rocking-core systems.

This paper aims to investigate the seismic performance of the controlled rocking steel braced frame equipped with yielding fuses and replaceable fuses under near-field ground motions compared to the far-field earthquakes. Previous studies showed that the rocking-core systems such as rocking steel braced frames with friction dampers (Roke *et al.* 2006) and yielding fuses (Eatherton and Hajjar 2010, Rahgozar *et al.* 2016a) are capable of reducing damage under far-field records by directing damage to replaceable devices. However, unlike far-field ground motions, when a fault ruptures towards a site at a speed close to the shear wave velocity, a distinct large pulse of near-field earthquakes imposes a large amount of seismic energy to the structures in a short time interval (Somerville *et al.* 1997). Hence, rocking-core systems may experience severe structural damage under near-field ground motions. Despite the research efforts on the self-centering systems, only few studies (e.g., Rahgozar *et al*. 2016b) have been reported recently on the assessment of controlled-rocking systems under near-field records. Therefore, a comparative study seems to be necessary to examine the efficiency of the self-centering system under far-field and near-field ground motions. The main objective of this paper is to evaluate the seismic performance of a dual-configuration self-centering braced frame [Fig. 1(I)] under a set of near-field pulse-like (NF-pulse) ground motion. The following sections review the configuration, mechanical behavior, and seismic design method of the rocking braced frame and discuss its seismic performance from various different through nonlinear time history analysis.

## 2. Overview of mechanical behavior and design of self-centering braced frame

A team from Lehigh University introduced dual-configuration rocking-core braced frame (Eatherton and Hajjar 2010). Eatherton and Hajjar (2010) and Ma *et al.* (2011) have introduced and conducted experimental tests on 4-story (half scale) and 3-story (two-third scale) rocking braced frames, respectively. Fig. 1(I) shows the controlled-rocking braced frame equipped with PT cables and replaceable yielding fuses. PT strands are restrained upright to top and bottom of the frame, and replaceable fuses are located in the middle bay between the frames. The rocking frame is isolated vertically, which makes it possible to sway on its foundation during an earthquake. Eatherton and Hajjar (2010) performed the similar system equipped with different

∗Corresponding author, Professor
E-mail: Moghadam@iiees.ac.ir
[a]Ph.D.
[b]Ph.D.

**Copyright © 2017 Techno-Press, Ltd.**

ISSN: 1225-4568 (Print), 1598-6217 (Online)

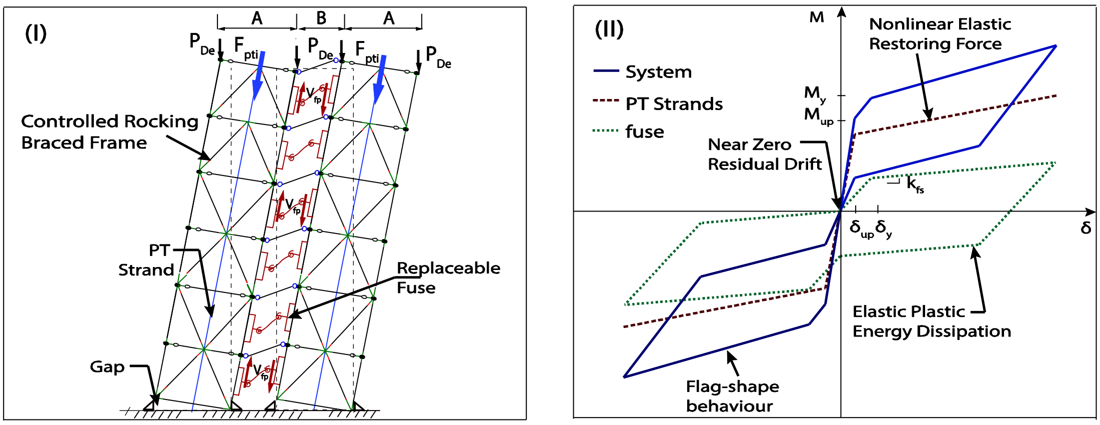


Fig. 1 (I) Self-centering steel-braced frame. (II) An idealized flag-shape curve of the system and hysteretic curves of the fuse and PT strand

combinations of fuses and post-tensioning and refine construction details for the rocking system. Hall *et al.* (2010) were conducted computational studies to investigate the effect of modeling parameter under far-field ground motions. Eatherton *et al.* (2014) presented design concepts and Rahgozar *et al.* (2016c) have quantified the seismic performance factors for controlled rocking steel-braced frames.

Fig. 1(II) shows the behaviors of the self-centering system, PT cables, and fuses. PT strands provide restoring force fuses ensure the required energy dissipation for the rocking system. As shown in Fig. 1(I), the flag-shape behavior of the system consists of three main branches. The first is the linear elastic branch that terminates when the system initiates to uplift ($M_{up}$) and then follows to the system yielding point ($M_y$) by a hardening branch, which is the beginning of the post-yield hardening branch. The amount of uplift moment, $M_{up}$, and yield moment, $M_y$, are the function of post-tensioning force, gravity loads, and fuse force. Once the lateral overturning moment overcame resisting moment force ($M \geq M_{up}$) provided by the PT strands and fuses, the braced frame uplift and a base joint gap opened. At the decompression ($M_{up} < M \leq M_y$) the stiffness of the rocking frame significantly reduced, which is provided by the elastic stiffness of the frame and fuses. This stiffness reduction leads to period lengthens of the system and reduces structural damage by limiting applied forces to the rocking system. In the third branch of the flag-shape system, the post-yield stiffness of the system is composed frame stiffness and fuse hardening stiffness. When the lateral forces are decreased and frame unloaded, fuses dissipate input energy through yielding.

Eatherton *et al.* (2014) introduced limit states design procedure for design of self-centering braced frame which is implemented in this paper. According to this method, using equivalent lateral force (ELF) method (ASCE 2010), the minimum required strength for the system and its components is determined. Following the calculation of applied overturning moment ($M_u$), initial post-tensioning force ($F_{pti}$) and required shear fuse capacity ($V_{fp}$) are computed by the following equations

$$V_{fp} \geq \frac{Mu}{\phi(1+SC)(A+B)}; \qquad \phi = 0.9 \tag{1}$$

$$F_{pti} \geq 젤 \frac{Mu}{\phi(1+SC)} \frac{SC}{A} - \phi P_{De}; \qquad \phi = 0.9 \tag{2}$$

where $P_{De}$ is the tributary gravity loads. A is the bay width of the frame and B is the middle bay width between the frames [Figs. 1(I) and 2]. SC denotes the capability of the system to provide self-centering feature, which could be adjusted by the following equation

$$SC = \frac{\sum \frac{A}{2} \times \left(F_{pti} + 2P_{De}\right) + k_{fs} \times \delta_{up}}{\sum (A+B) \times V_{fp}} \geq 1 \tag{3}$$

The required cross-sectional area of *PT* strands ($A_{PT}$) could be designed by Eq. (4) in terms of frame configuration, material properties, $F_{pti}$, and target PT post-straining ($\varepsilon_{target}$) provided by initial PT strain ($\varepsilon_{pti}$) and an applied strain at the roof drift ratio ($RDR_{target}$)

$$A_{PT} = \frac{F_{pti}}{\left(\varepsilon_{target} - \frac{A \times RDR_{target}}{2L_{PT}}\right) E_{PT}} \tag{4}$$

Note that the *PT* area should be adjusted so that the $\varepsilon_{target}$ of *PT* does not exceed the *PT* strain limit ($\varepsilon_{limit}$) at the $RDR_{target}$. Value of $\varepsilon_{\mathrm{limit}}$ depends on the type of material and PT anchorage systems (walsh and Kurama 2012).

In order to provide required shear fuse capacity, $V_{fP}$, the fuses are designed by the following equation (Ma *et al.* 2010)

$$N_{fs} Nl_{fs} = \frac{?.25\mathrm{V}_{\mathrm{fp}} \times \mathrm{l}_{\mathrm{fs}}?}{\mathrm{f}_{\mathrm{y,fs}} \times \mathrm{t}_{\mathrm{fe}} \times b_{\mathrm{fs}}^2 ?} \tag{5}$$

where $N_{fs}$ and $Nl_{fs}$ are a number of required fuses and links, respectively, and $l_{fuse}$, $t_{fuse}$, $b_{fuse}$ denote fuse geometry. $f_{y,fs}$ is the yield strength of fuse material.

The energy dissipation capacity of the system provided

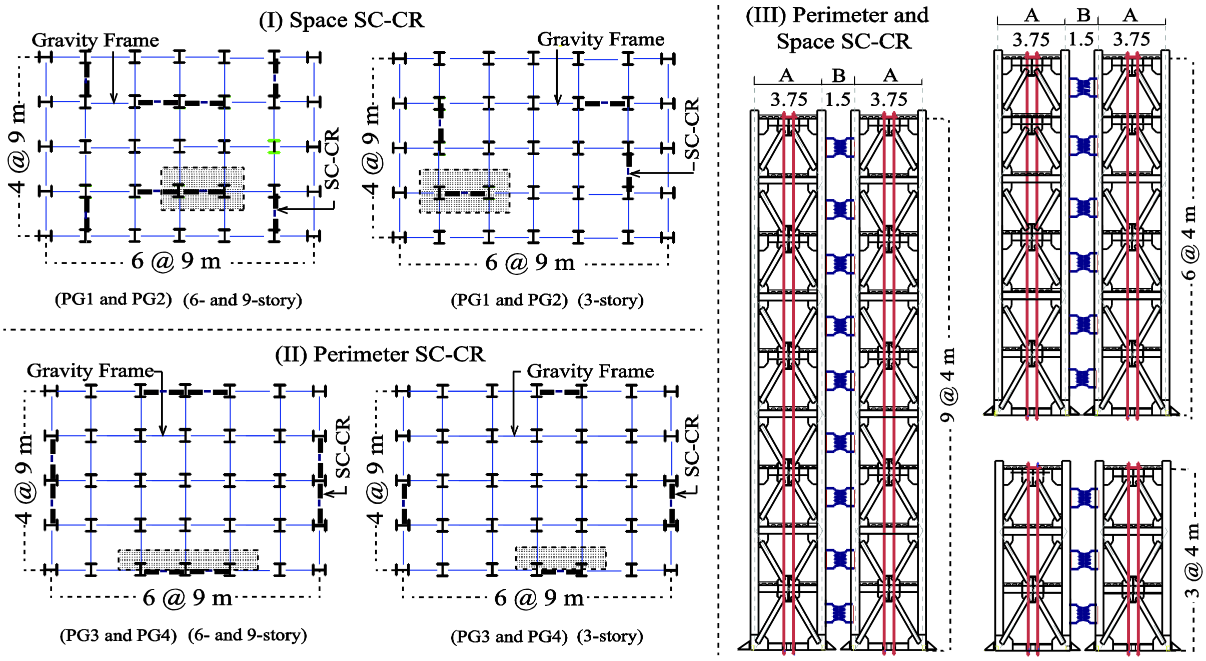


Fig. 2 Plan and elevation of self-centering braced frame archetypes

by fuses should be examined as follows

$$ED \cong \frac{\sum V_{fp}\left(A+B\right)}{M_y} \geq 0.25 \tag{6}$$

And, the global uplift of the controlled-rocking braced must be prevented by controlling the following equation

$$UL = \frac{\sum F_{pti} + \sum P_{De}}{\sum V_{fp}} \geq 1 \tag{7}$$

## 3. Performance groups and seismic design of controlled-rocking archetypes

The 4×6 bays office building of the project of seismic design criteria for steel moment frame construction (SAC steel project) (Gupta and Krawinkler 1999) is considered as a prototype building. The dead/live loads and seismic mass of each floor are 9459/1974 kN and 1033 kN.sec$^2$/m, respectively. Four performance groups, PGs, consist of twelve rocking archetypes are selected and designed. Fig. 2 shows the configuration of the archetypes, which are categorized in terms of a number of stories, seismic frame type (space/perimeter), and seismic design categories, SDC, as shown in Table 1. There are two archetypes in each direction of three-story buildings, and four braced frames for six- and nine-story buildings. The spanning ratio (A/B) and story height of archetypes are equal to 2.5 and 4 m, respectively. It is further assumed that the archetypes are located near Los Angeles, California. The archetypes are designed for soil site class *D* with two *SDC* (that is $S_{D1}$=1 g and $S_{Ds}$=0.6 g for *SDC* $D_{\max}$ and $S_{D1}$=0.49 g and $S_{Ds}$=0.19 g for *SDC* $D_{\min}$).

Using procedure introduced in Section 2, the archetypes are designed for the high and low seismicity regions with soil site class D. Some of the design results are summarized in Table 1.The required moment strength of the archetypes is first computed using the ELF method with response modification factor, $R$=8. The shear strength of fuse, $V_{fp}$, and initial post-tensioning force, $F_{pti}$, are calculated using Eqs. (1) and (2), respectively. As listed in Table 1, $F_{pti}$ and $V_{fp}$ range from 249 to 7256 kN, and from 96 to 318 kN, respectively.

Assuming $\varepsilon_{\text{limit}}$=0.8% and $RDR_{target}$=2%, $A_{PT}$ and $N_{PT}$ are designed by Eq. (4) for PT cables with modulus of elasticity, $E_{PT}$=193.06 kN/mm, nominal ultimate strength, $f_{uPT}$=2.18 kN/mm$^2$, and nominal yield strength, $f_{yPT}$=1.73 kN/mm$^2$. As shown in Table 1, the required $A_{PT}$ for the archetypes ranges between 260 and 2800 mm$^2$ and equivalent $N_{PT}$ strands ranges from 2 to 30. The $N_{fs}$ and $Nl_{fs}$ of butterfly-shaped fuses are designed by Eq. (5). Thickness ($t$) and slenderness ratio ($L/t$) of each fuse are equal to 31.7 mm and 22.4, respectively. The designed $N_{fs}$ and $Nl_{fs}$ are in the ranges of 6-18 and 1-4, respectively, as shown in Table 1. Finally, to control design properties of the archetypes, self-centering, uplift, and energy dissipation ratio are determined using Eqs. (3), (6) and (7) and compared to their limit values.

## 4. Modeling of self-centering archetypes

Numerical modeling and a non-linear time history analysis are carried out using OpenSees software (2011). Fig. 3 shows a detailed scheme of the two-dimensional modeling of the archetype. The rocking braced frames are modeled using nonlinear 'steel-02' material and

Table 1 Design results of self-centering braced frame archetypes.

| | $D_{max}$/Perimeter | | | $D_{min}$/Perimeter | | | $D_{max}$/Space | | | $D_{min}$/Space | | |
|---|---|---|---|---|---|---|---|---|---|---|---|---|
| | $R_{31}$ | $R_{61}$ | $R_{91}$ | $R_{32}$ | $R_{62}$ | $R_{92}$ | $R_{33}$ | $R_{63}$ | $R_{93}$ | $R_{34}$ | $R_{64}$ | $R_{94}$ |
| | 3-st. | 6-st. | 9-st. | 3-st. | 6-st. | 9-st. | 3-st. | 6-st. | 9-st. | 3-st. | 6-st. | 9-st. |
| $F_{Pti}$ (kN) | 2062 | 3689 | 7256 | 768 | 743 | 1345 | 1543 | 2652 | 3305 | 249 | 300 | 425 |
| $A_{PT}$ (cm$^2$) | 22 | 28 | 26 | 8.3 | 5.7 | 9.7 | 16.8 | 20 | 41 | 2.7 | 2.6 | 3.1 |
| $N_{PT}$ | 16 | 20 | 30 | 6 | 4 | 7 | 12 | 15 | 30 | 2 | 2 | 2 |
| $V_{fP}$(kN) | 280 | 256 | 318 | 139 | 96 | 105 | 280 | 256 | 318 | 139 | 96 | 105 |
| $N_{fs}$ -$N_{lfs}$ | 3-8 | 6-8 | 9-10 | 3-4 | 3-4 | 3-6 | 3-8 | 6-8 | 9-10 | 3-4 | 3-4 | 3-6 |

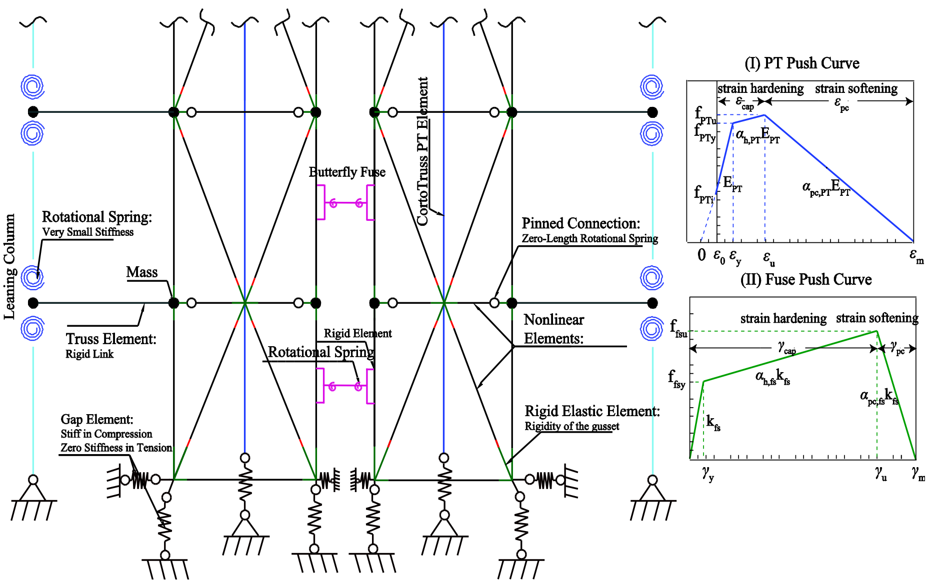


Fig. 3 Nonlinear modeling of self-centering braced frame in Opensees

‘displacement beam-column’ fiber elements. Two leaning columns are modeled using ‘elastic beam column’, ‘zero-stiffness spring’ elements, and ‘rigid truss’ elements to simulate the effect of the geometric nonlinearities. ‘Elastic-No Tension’ material with ‘zero-length’ elements are implemented for modeling the gap opening of boundary conditions of the system. The braces are modeled using 10 fiber elements with the initial geometrical imperfection to capture probable in-plane brace buckling. The gusset plates of braces are also modeled using ‘force-based beam-column’ and ‘elastic beam column’ elements, to simulate their global and local behaviors as the modeling method discussed in Uriz and Mahin’s (2004) study. As shown in Fig. 3(I), post-tensioning strands are modeled using a series combination of ‘elasticPP’ and ‘hysteretic’ materials with ‘corotational truss’ elements. Non-degrading fuses are explicitly made using ‘elastic beam column’, fiber ‘disp. beam column’, and ‘rotational spring’ elements to simulate their accurate flexural, axial, and lateral torsional buckling behaviors. Fig. 3(II) shows the ideal backbone curve of fuse material which is implemented using a series combination of ‘steel-02’ and ‘hysteretic’ materials.

## 5. Non-linear dynamic analysis

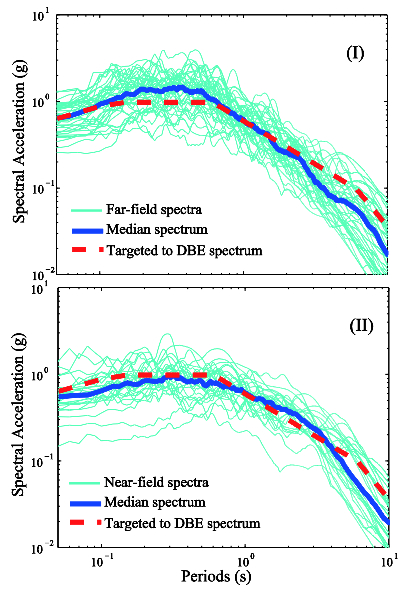


Fig. 4 (I) far-field and (II) near-field pulse-like records at DBE level for 3-story archetype located in SDC $D_{max}$

### *5.1 Far-fault and near-field pulse like ground motions*

Nonlinear time history analyses are performed to quantify the engineering demand parameters (EDPs) of

Table 2 Dataset of the far-field and near-field ground motion records (FEMA 2009)

| | | | Far-field records | | Near-field pulse-like records | |
|---|---|---|---|---|---|---|
| ID | Event | Year | Station | $PGA_{max}(g)$* | Station | $PGA_{max}(g)$* |
| 1 | Northridge | 1994 | Beverly Hills Mulhol | 0.52 | Rinaldi Receiving Sta | 0.87 |
| 2 | Northridge | 1994 | Canyon W Lost Cany | 0.48 | Sylmar - Olive View | 0.73 |
| 3 | Duzce, Turkey | 1999 | Bolu | 0.82 | Duzce | 0.52 |
| 4 | Hector Mine | 1999 | Hector | 0.34 | - | - |
| 5 | Imperial Valley | 1979 | Delta | 0.35 | - | - |
| 6 | Imperial Valley | 1979 | El Centro Array#11 | 0.38 | El Centro Array #6 | 0.44 |
| 7 | Kobe, Japan | 1995 | Nishi-Akashi | 0.51 | El Centro Array #7 | 0.46 |
| 8 | Kobe, Japan | 1995 | Shin-Osaka | 0.24 | - | - |
| 9 | Kocaeli,Turkey | 1999 | Duzce | 0.36 | Izmit | 0.22 |
| 10 | Kocaeli,Turkey | 1999 | Arcelik | 0.22 | - | - |
| 11 | Erzican, Turkey | 1992 | - | - | Erzincan | 0.49 |
| 12 | Landers | 1992 | Yermo Fire Station | 0.24 | - | - |
| 13 | Landers | 1992 | Coolwater | 0.42 | Lucerne | 0.79 |
| 14 | Loma Prieta | 1989 | Capitola | 0.53 | Saratoga - Aloha | 0.38 |
| 15 | Loma Prieta | 1989 | Gilroy Array #3 | 0.56 | - | - |
| 16 | Manjil, Iran | 1990 | Abbar | 0.51 | - | - |
| 17 | Superstition Hills | 1987 | El Centro Imp. Cent | 0.36 | Parachute Test Site | 0.42 |
| 18 | Superstition Hills | 1987 | Poe Road (temp) | 0.45 | - | - |
| 19 | Cape Mendocino | 1992 | Rio Dell Overpass far-field | 0.55 | Petrolia | 0.63 |
| 20 | Chi-Chi, Taiwan | 1999 | CHY101 | 0.44 | TCU065 | 0.82 |
| 21 | Chi-Chi, Taiwan | 1999 | TCU045 | 0.51 | TCU102 | 0.29 |
| 22 | San Fernando | 1971 | LA - Hollywood Stor | 0.21 | - | - |

*Maximum PGA of two horizontal components

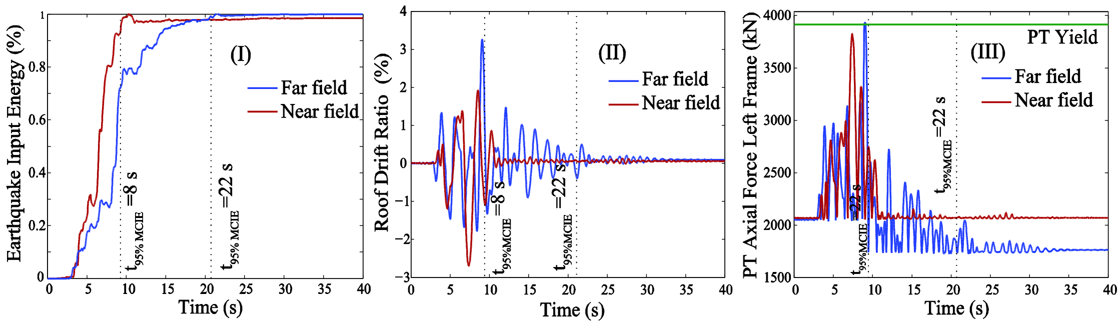


Fig. 5 (I) Cumulative energy input, (II) roof drift ratio, and (III) PT axial force of $R_{31}$ archetype under targeted far-field (Beverly Hills station) and NF-pulse (Sylmar station) records of Northridge Earthquake, 1994 to DBE

rocking archetypes under far- and near-field ground motions. Table 2 shows the far-field and near-field pulse like ground motion set adapted from Fema-P695 (FEMA 2009). The nonlinear analyses are conducted at the design basis earthquake (DBE) and maximum credible earthquake (MCE) intensity levels (10 and 2% probability of exceedance in 50 years). For this purpose, according to proposed method in Fema P695 (FEMA 2009), the ground motions are first normalized, and then the median spectral acceleration is determined by fitting a lognormal distribution to the normalized spectral acceleration.

The scaling factor to scale the median spectra to target spectra (DBE and MCE) is then computed at the fundamental period of each archetype. Fig. 4 shows samples of targeted spectra of scaled records to design base earthquake for 3-story archetype located at seismic design category $D_{max}$.

### *5.2 Nonlinear analysis results*

To compare the dynamic responses of rocking archetypes under targeted far- and near-field ground motions to DBE and MCE, results of analyses are quantified in terms of key engineering demand parameters,

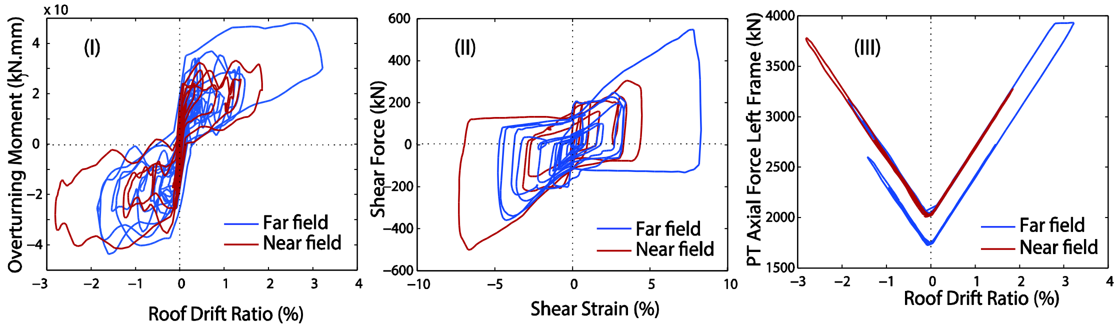


Fig. 6(I) Overturning moment-roof drift ratio, (II) shear force-shear strain of fuses, and (III) PT axial force-roof drift ratio of $R_{31}$ archetype under far-field and NF-pulse records of Northridge Earthquake at DBE level

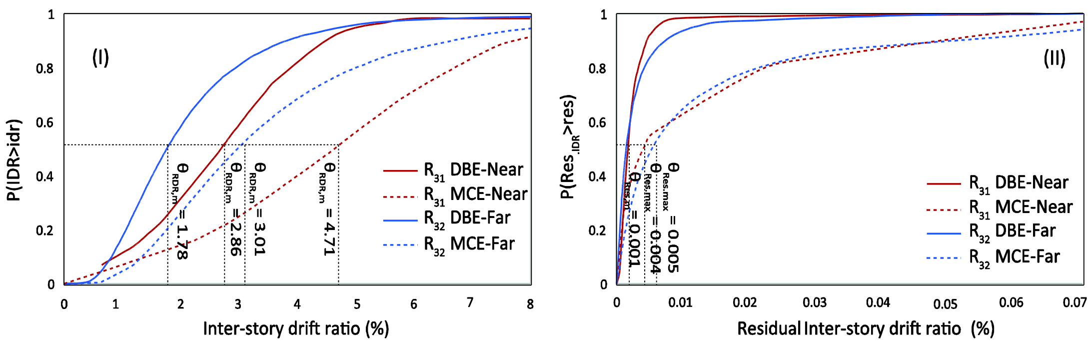


Fig. 7 Cumulative distributions of (I) maximum and (II) residual inter-story drift ratio for the three-story $R_{31}$ archetypes subjected to far- and near-field ground motions

as shown in Table 3. Note that n-storey rocking archetypes in the ith PG is called $R_{nSt.Pgi}$.

Fig. 5 represents cumulative input energy (CIE), roof drift ratio (*RDR*), and *PT* axial force for $R_{31}$ archetype subjected to the scaled far-field (Beverly Hills station) and NF-pulse (Sylmar station) records of Northridge Earthquake, 1994. As shown in Fig. 5(I), unlike NF-pulse case, more time ($t_{95\%MCIE}$) is spent to impose most of the seismic energy (i.e., 95% of maximum CIE) to the archetype under far-field record. In this example, $t_{95\%MCIE}$ for far-field and NF-pulse cases are 22 and 8 s, respectively, indicating the impulsive nature of NF-pulse ground motions.

Figs. 5(II) and 5(III) show the RDR and PT axial force of the representative examples. As shown, the archetype sustained large displacement cycles [Figs. 5(II)] and high *PT* axial force [Figs. 5(III)] in the short time ($t_{95\%MCIE}$<8 s) at the beginning of the NF-pulse record, while the responses almost uniformly distributed under the far-field record. Moreover, although the PT restoring force is decreased due to *PT* yield [Figs. 5(III)] under far-field case, Figs. 5(II) indicates the ability of the rocking archetype on preventing residual *RDR* at the end of both far- and near-field ground motions. This feature of the rocking archetype helps the system to experience less structural and permanent damage at the end of a severe earthquake.

Fig. 6 shows the examples of *PT* axial force versus RDR, fuse shear force versus fuse shear strain, and overturning moment versus *RDR* for R31 archetype under scaled far- and near-fault records of Northridge Earthquake, 1994. Fig. 6(I) indicates the identical trend of flag-shape responses and reversibility of the archetype under both types of considered earthquakes. Although, a low number of cycles is required to reach maximum demands of the archetype under NF-pulse record, the proper behavior of the system on dissipating the seismic energy of far- and near-fault records through the stable response of the fuse is evident in Fig. 6(II). It can be also seen from Figs. 6(I) and 6(III) that the *PT* yield of archetype under far-field record at the 2.5% *RDR* caused minimal residual drift.

Fig. 7 shows examples of the fragility curves of maximum *EDP* ($\theta_{EDP}$) for the 3-storey archetypes subjected to far-field and NF-pulse records. The curves are log-normal cumulative $R_{31}$ distributions fitted on the $\theta_{EDP}$. The *y*-axis denotes the probability of exceeding a given *EDP* at a desired intensity measure, *IM*, ($P(\theta_{EDP}>\theta_{edp}\ |IM)$). The 50% probability (median) of occurrence of a $\theta_{EDP}$ named $\theta_{EDP,m}$ is defined here as an index to compare responses of archetypes. The mean maximum of inter-storey drift ratio ($\theta_{IDR,m}$), net inter-story drift ($\theta_{net.IDR,m}$; i.e., flexural drift), residual *IDR* ($\theta_{Res.IDR,m}$), *PT* strain ($\theta_{PT\text{-}Strrain,m}$), fuse strain ($\theta_{fuse\text{-}Strrain,m}$), and roof acceleration ($\theta_{roof\text{-}acc,m}$) of rocking archetypes under both targeted far- and near-field records to *DBE* and *MCE* levels summarized in Table 3. As shown, $\theta_{IDR,m}$ values are 0.5 to1.97% and 0.54 to 3.07% under far- and near-field records, respectively, which are less than the of 2 and 3% *IDRs* limits at *DBE* and *MCE* levels. Moreover, $\theta_{net.IDR,m}$, resulting structural member deflection, under far- and near-field are in the range of 0.05-0.71% and 0.05-0.43%, respectively; and $\theta_{Res.IDR,m}$ of archetypes equal to 0.0042-0.275% and 0.005-0.15%, under far- and near-field,

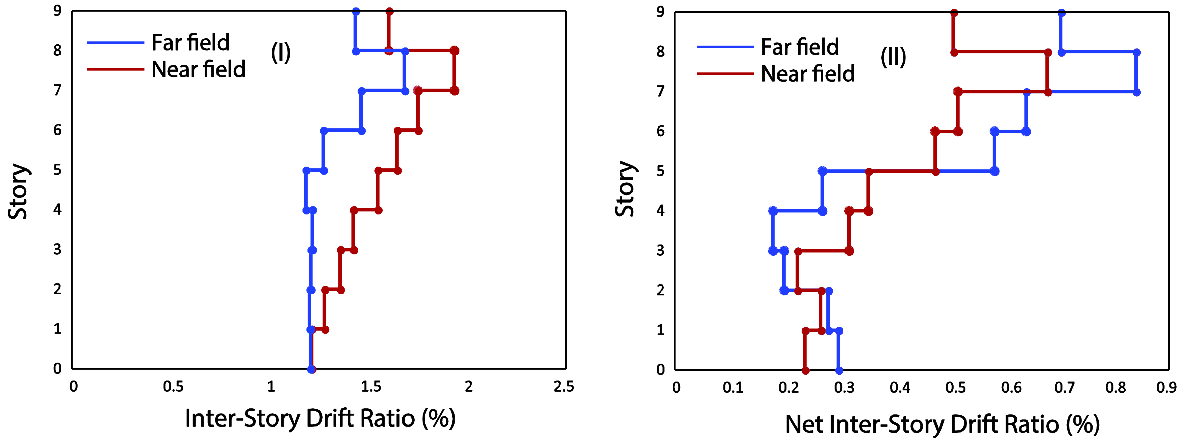


Fig. 8 Distribution of (I) maximum inter-story drift ratios and (II) net inter-story drift ratios for R91 archetype under targeted far-field (Beverly Hills) and NF-pulse (Sylmar) records of Northridge Earthquake, 1994 to DBE level

respectively, indicating that residual drift of rocking archetypes under both types of earthquakes is negligible. Note that $\theta_{Res.IDR}$ of the rocking archetypes is less than the 0.5 and 1.0% limit values defined by ATC-P58 (ATC 2004), for identifying the need for structures to be repaired and rebuilt, respectively.

## 6. Sensitivity study

A sensitivity analysis is conducted to examine the effects of ground motion and modeling parameters on the $\theta_{EDP,m}$.

### *6.1 Effects of modeling parameters*

For a detailed comparison, Fig. 8 shows the distribution of $\theta_{IDR}$ and $\theta_{net.IDR}$ of $R_{91}$ archetype under NF-pulse and far-field records of Northridge earthquake. As shown, $\theta_{IDR}$ values of the archetype under the NF-pulse case are larger than those for the far-field case [Fig. 8(a)]. However, $\theta_{net.IDR}$ is not distributed uniformly along the height [Fig. 8(b)] and their values for middle and upper stories of the archetype under the far-field record are lower and higher than the NF-pulse record, respectively. The $\theta_{net.IDR}$ variation can be attributed to the effective duration of each earthquake type, at which most of the seismic energy is entered into the archetypes. Therefore, NF-pulse records caused lower $\theta_{net.IDR}$ compared with far-field records (Table 3) due to their lower duration in the finite range of pulse period. As a result, structural damage probability of rocking archetypes under far-field earthquake is higher than those of the NF-pulse ones. Moreover, it is observed that the $\theta_{roof\text{-}acc}$ values of archetypes under far-field records is higher than those of the NF-pulse ones, which can cause more damage to block-type non-structural components.

Fig. 9 indicates the effects of number of stories, seismic frame type and *SDC* parameters on $\theta_{RDR}$, $\theta_{net.IDR}$, and $\theta_{acc}$ for the both considered earthquake types. As can be seen, $\theta_{IDR}$ of the archetypes are decreased by increasing the structural height, while $\theta_{acc}$ and $\theta_{net.IDR}$ values are increased as the height increases. It can also be observed that $\theta_{RDR}$ values for space archetypes ($PG_3$ and $PG_4$) are higher than those of perimeter ones ($PG_1$ and $PG_2$), but their $\theta_{net.IDR}$ and $\theta_{acc}$ are lower than perimeter archetypes. This issue indicates that the damage probability of space frames is lower than perimeter ones, which can be related to the effective gravity load attributed to perimeter frame with respect to the space one. Moreover, $\theta_{EDP}$ values are larger for archetypes located at $SDC\ D_{\max}$ ($PG_1$ and $PG_3$) than for those at $SDC\ D_{\min}$ ($PG_2$ and $PG_4$).

### *6.2 Effects of ground motion parameters*

For examining the effect of hazard intensity and earthquake type, indices of intensity, $I_s$, and earthquake type, $I_{eq.}$, resulting from the $\theta_{EDP,m}$ are defined as follows

$$I_s = \frac{(\theta_{EDP})_{MCE}}{(\theta_{EDP})_{DBE}} \tag{8}$$

$$I_{eq.} = \frac{(\theta_{EDP})_{Near-feild}}{(\theta_{EDP})_{Far-feild}} \tag{9}$$

where; $I_s$ is denotes the ratio of $\theta_{EDP}$ value under MCE to DBE level and $I_{eq.}$ is the ratio of $\theta_{EDP}$ value for the archetype under NF-pulse to far-field records.

$I_s$ and $I_{eq.}$ values and their mean for all the archetypes are listed in Table 3. As can be seen, the $\theta_{IDR}$, $\theta_{net.IDR}$, $\theta_{Res.IDR}$, $\theta_{roof\text{-}acc}$, $\theta_{PT\text{-}Strrain}$, $\theta_{fuse\text{-}Strrain}$ of archetypes at MCE level are about 1.65, 1.30, 1.26, 1.25, 1.88, and 1.74 times of DBE intensity, respectively. Although it is clear that $\theta_{EDP}$ of archetypes at MCE intensity are higher than that of DBE level, the rate of increase under far-field earthquakes is larger than that of the near-field ones. Moreover, $\theta_{IDR}$, $\theta_{net.IDR}$, $\theta_{Res.IDR}$, $\theta_{roof\text{-}acc}$, $\theta_{PT\text{-}Strrain}$, and $\theta_{fuse\text{-}Strrain}$ under NF-pulse record set are about 1.34, 0.82, 1.08, 0.95, 1.42, and 1.39 times of the far-field records, respectively. This issue indicates that the near-fault earthquakes may impose larger demands compared to far-field records.

Table 3 results of processed engineering demand parameters

| | | | $D_{max}$/Perimeter | | | $D_{min}$/Perimeter | | | $D_{max}$/Space | | | $D_{min}$/Space | | | mean |
|---|---|---|---|---|---|---|---|---|---|---|---|---|---|---|---|
| | | | $R_{31}$ | $R_{61}$ | $R_{91}$ | $R_{32}$ | $R_{62}$ | $R_{92}$ | $R_{33}$ | $R_{63}$ | $R_{93}$ | $R_{34}$ | $R_{64}$ | $R_{94}$ | |
| | | | 3-st. | 6-st. | 9-st. | 3-st. | 6-st. | 9-st. | 3-st. | 6-st. | 9-st. | 3-st. | 6-st. | 9-st. | |
| $\theta_{IDR,m}$ (%) | DBE | F[a] | 1.68 | 1.33 | 1.36 | 0.64 | 0.5 | 0.51 | 1.97 | 1.62 | 1.56 | 0.79 | 0.58 | 0.53 | 1.09 |
| | | N[b] | 2.66 | 1.83 | 1.46 | 1.25 | 0.7 | 0.55 | 3.07 | 1.85 | 1.72 | 1.45 | 0.72 | 0.54 | 1.48 |
| | | $I_{eq.}$[c] | 1.58 | 1.38 | 1.07 | 1.95 | 1.40 | 1.08 | 1.56 | 1.14 | 1.10 | 1.84 | 1.24 | 1.02 | 1.36 |
| | MCE | F | 2.96 | 2.46 | 2.17 | 1.19 | 0.85 | 0.84 | 3.32 | 2.56 | 2.27 | 1.32 | 0.97 | 0.91 | 1.82 |
| | | N | 4.6 | 2.86 | 2.25 | 2.31 | 1.01 | 0.73 | 4.93 | 2.94 | 2.89 | 2.42 | 1.21 | 1.03 | 2.43 |
| | | $I_{eq.}$ | 1.55 | 1.16 | 1.04 | 1.94 | 1.19 | 0.87 | 1.48 | 1.15 | 1.27 | 1.83 | 1.25 | 1.13 | 1.32 |
| | $I_S$[d] | F | 1.77 | 1.85 | 1.60 | 1.86 | 1.70 | 1.65 | 1.69 | 1.58 | 1.46 | 1.67 | 1.67 | 1.72 | 1.68 |
| | | N | 1.73 | 1.56 | 1.54 | 1.85 | 1.44 | 1.33 | 1.61 | 1.59 | 1.68 | 1.67 | 1.68 | 1.91 | 1.63 |
| $\theta_{net\text{-}IDR,m}$ (%) | DBE | F[a] | 0.18 | 0.33 | 0.52 | 0.07 | 0.13 | 0.17 | 0.15 | 0.29 | 0.45 | 0.05 | 0.09 | 0.12 | 0.21 |
| | | N[b] | 0.17 | 0.27 | 0.39 | 0.07 | 0.12 | 0.11 | 0.15 | 0.22 | 0.25 | 0.05 | 0.06 | 0.08 | 0.16 |
| | | $I_{eq.}$ | 0.94 | 0.82 | 0.75 | 1.00 | 0.92 | 0.65 | 1.00 | 0.76 | 0.56 | 1.00 | 0.67 | 0.67 | 0.81 |
| | MCE | F | 0.22 | 0.43 | 0.71 | 0.07 | 0.15 | 0.23 | 0.2 | 0.39 | 0.68 | 0.06 | 0.12 | 0.18 | 0.29 |
| | | N | 0.22 | 0.32 | 0.43 | 0.08 | 0.13 | 0.13 | 0.21 | 0.28 | 0.33 | 0.07 | 0.1 | 0.12 | 0.20 |
| | | $I_{eq.}$ | 1.00 | 0.74 | 0.61 | 1.14 | 0.87 | 0.57 | 1.05 | 0.72 | 0.49 | 1.17 | 0.83 | 0.67 | 0.82 |
| | $I_S$ | F | 1.22 | 1.30 | 1.37 | 1.00 | 1.15 | 1.35 | 1.33 | 1.34 | 1.51 | 1.20 | 1.33 | 1.50 | 1.30 |
| | | N | 1.29 | 1.19 | 1.10 | 1.14 | 1.08 | 1.18 | 1.40 | 1.27 | 1.32 | 1.40 | 1.67 | 1.50 | 1.30 |
| $\theta_{Res\text{-}IDR}$ $(\times 10^{-3})$ | DBE | F[a] | 1.23 | 1.14 | 0.68 | 0.47 | 0.12 | 0.14 | 0.91 | 0.66 | 0.37 | 0.11 | 0.05 | 0.05 | 0.49 |
| | | N[b] | 1.13 | 1.08 | 0.80 | 0.46 | 0.12 | 0.21 | 1.41 | 0.77 | 0.49 | 0.15 | 0.06 | 0.05 | 0.56 |
| | | $I_{eq.}$ | 0.92 | 0.95 | 1.19 | 0.98 | 1.00 | 1.57 | 1.55 | 1.16 | 1.33 | 1.38 | 1.17 | 1.06 | 1.19 |
| | MCE | F | 2.75 | 0.98 | 1.45 | 0.46 | 0.12 | 0.42 | 1.91 | 0.65 | 0.86 | 0.28 | 0.08 | 0.11 | 0.84 |
| | | N | 1.53 | 1.14 | 0.74 | 0.71 | 0.11 | 0.18 | 1.19 | 0.75 | 0.43 | 0.53 | 0.13 | 0.09 | 0.63 |
| | | $I_{eq.}$ | 0.56 | 1.16 | 0.51 | 1.55 | 0.93 | 0.44 | 0.62 | 1.15 | 0.50 | 1.94 | 1.68 | 0.78 | 0.99 |
| | $I_S$ | F | 2.23 | 0.86 | 2.15 | 0.98 | 1.00 | 3.06 | 2.10 | 0.98 | 2.34 | 2.54 | 1.58 | 2.41 | 1.85 |
| | | N | 1.35 | 1.05 | 0.93 | 1.55 | 0.93 | 0.86 | 0.85 | 0.97 | 0.89 | 3.56 | 2.29 | 1.78 | 1.42 |
| $\theta_{PT\text{-}Strain,m}$ | DBE | F[a] | 0.2 | 0.05 | 0.05 | 0.08 | 0.02 | 0.01 | 0.28 | 0.1 | 0.05 | 0.12 | 0.04 | 0.02 | 0.09 |
| | | N[b] | 0.37 | 0.08 | 0.04 | 0.18 | 0.04 | 0.01 | 0.46 | 0.11 | 0.04 | 0.22 | 0.04 | 0.02 | 0.13 |
| | | $I_{eq.}$ | 1.85 | 1.60 | 0.80 | 2.25 | 2.00 | 1.00 | 1.64 | 1.10 | 0.80 | 1.83 | 1.00 | 1.00 | 1.41 |
| | MCE | F | 0.41 | 0.15 | 0.06 | 0.14 | 0.05 | 0.02 | 0.53 | 0.16 | 0.08 | 0.19 | 0.07 | 0.03 | 0.16 |
| | | N | 0.69 | 0.17 | 0.06 | 0.36 | 0.07 | 0.02 | 0.69 | 0.16 | 0.08 | 0.43 | 0.1 | 0.04 | 0.24 |
| | | $I_{eq.}$ | 1.68 | 1.13 | 1.00 | 2.57 | 1.40 | 1.00 | 1.30 | 1.00 | 1.00 | 2.26 | 1.43 | 1.33 | 1.43 |
| | $I_S$ | F | 2.05 | 3.00 | 1.20 | 1.75 | 2.50 | 2.00 | 1.89 | 1.60 | 1.60 | 1.58 | 1.75 | 1.50 | 1.87 |
| | | N | 1.86 | 2.13 | 1.50 | 2.00 | 1.75 | 2.00 | 1.50 | 1.45 | 2.00 | 1.95 | 2.50 | 2.00 | 1.89 |
| $\theta_{fuse\text{-}Strain,m}$ | DBE | F[a] | 3.8 | 2.89 | 3.1 | 1.59 | 1.32 | 1.24 | 5.13 | 4.39 | 4.01 | 2.19 | 1.49 | 1.31 | 2.71 |
| | | N[b] | 6.64 | 4.44 | 3.57 | 3.27 | 2.05 | 1.42 | 7.67 | 4.62 | 4.97 | 3.84 | 2.27 | 1.62 | 3.87 |
| | | $I_{eq.}$ | 1.75 | 1.54 | 1.15 | 2.06 | 1.55 | 1.15 | 1.50 | 1.05 | 1.24 | 1.75 | 1.52 | 1.24 | 1.46 |
| | MCE | F | 7.41 | 6.64 | 5.46 | 2.56 | 2.61 | 2.21 | 9.27 | 6.84 | 5.51 | 3.2 | 3.66 | 3.11 | 4.87 |
| | | N | 11.54 | 7.35 | 5.63 | 5.93 | 2.98 | 2.31 | 11.03 | 7.1 | 5.65 | 7.65 | 3.69 | 2.91 | 6.15 |
| | | $I_{eq.}$ | 1.56 | 1.11 | 1.03 | 2.32 | 1.14 | 1.05 | 1.19 | 1.04 | 1.03 | 2.39 | 1.01 | 0.94 | 1.32 |
| | $I_S$ | F | 1.95 | 2.30 | 1.76 | 1.61 | 1.98 | 1.78 | 1.81 | 1.56 | 1.37 | 1.46 | 2.46 | 2.37 | 1.87 |
| | | N | 1.74 | 1.66 | 1.58 | 1.81 | 1.45 | 1.63 | 1.44 | 1.54 | 1.14 | 1.99 | 1.63 | 1.80 | 1.62 |
| $\theta_{Roof\text{-}acc.,m}$(g) | DBE | F[a] | 0.98 | 2.35 | 6.17 | 0.34 | 0.41 | 1.71 | 0.93 | 1.51 | 2.87 | 0.311 | 0.4 | 1.2 | 1.6 |
| | | N[b] | 0.77 | 2.45 | 6.27 | 0.35 | 0.39 | 1.73 | 0.76 | 1.55 | 2.93 | 0.31 | 0.3 | 1.5 | 1.6 |
| | | $I_{eq.}$ | 0.79 | 1.04 | 1.02 | 1.03 | 0.95 | 1.01 | 0.82 | 1.03 | 1.02 | 1.00 | 0.9 | 1.2 | 0.99 |
| | MCE | F | 1.42 | 3.35 | 9.24 | 0.47 | 0.61 | 1.93 | 1.40 | 1.85 | 2.94 | 0.47 | 0.5 | 1.5 | 2.1 |
| | | N | 1.13 | 3.12 | 9.81 | 0.50 | 0.539 | 1.87 | 1.10 | 1.55 | 2.93 | 0.44 | 0.3 | 1.5 | 2.0 |
| | | $I_{eq.}$ | 0.80 | 0.93 | 1.06 | 1.06 | 0.88 | 0.97 | 0.79 | 0.84 | 1.00 | 0.94 | 0.6 | 0.9 | 0.91 |
| | $I_S$ | F | 1.45 | 1.43 | 1.50 | 1.38 | 1.49 | 1.13 | 1.51 | 1.23 | 1.02 | 1.51 | 1.4 | 1.2 | 1.3 |
| | | N | 1.47 | 1.27 | 1.56 | 1.43 | 1.38 | 1.08 | 1.45 | 1.00 | 1.00 | 1.42 | 1.0 | 0.9 | 1.2 |

[a] N, near-field pulse-like ground motion.

[b] F, far-field ground motion.

[c] $$I_{eq} = \frac{(\theta_{EDP})_{Near-feild}}{(\theta_{EDP})_{Far-feild}}$$

[d] $$I_s = \frac{(\theta_{EDP})_{MCE}}{(\theta_{EDP})_{DBE}}$$

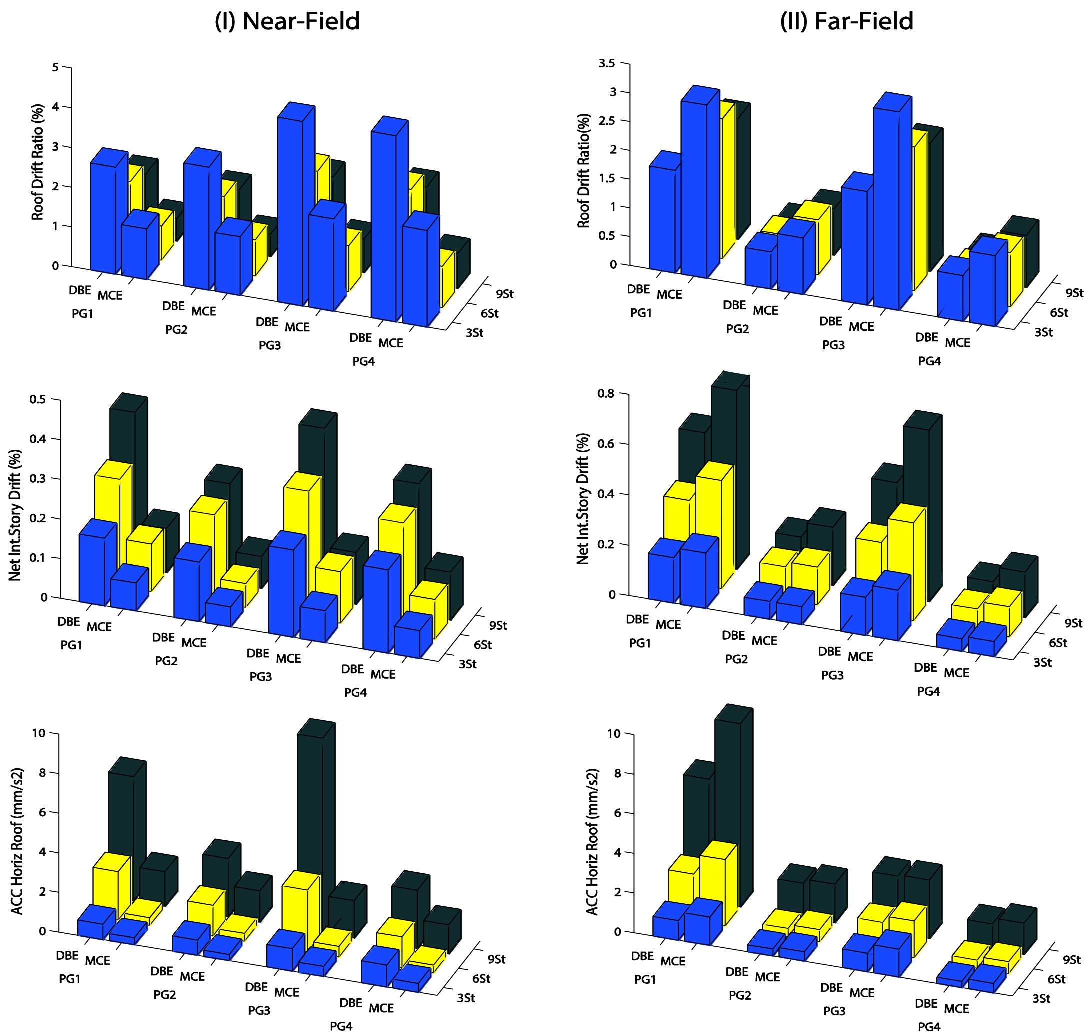


Fig. 9 Effects of the archetype height, seismic frame type, and seismic design category on the $\theta_{RDR}$, $\theta_{Net.IDR}$, and $\theta_{acc}$ of all archetypes under (I) NF-pulse and (II) far-field ground motions

## 9. Conclusions

Uniform structural damage as the common mechanism for conventional buildings may lead to costly repair after a severe earthquake. Rocking-core systems have been introduced to reduce damage through directing damage in replaceable devices. This paper has investigated the seismic performance and efficiency of the rocking braced frame subjected to near-field pulse-like ground motions (NF-pulse) compared to the far-field records. To this end, nonlinear dynamic analysis and sensitivity analysis were conducted to examine the effects of ground motion type and modeling parameters. Results of the investigation were compared in terms of intensity ($I_s$) and earthquake type ($I_{eq.}$) indices resulting from the median of maximum engineering demand parameters ($\theta_{EDP,m}$). The main conclusions of the investigation are as follows:

• It was found that median maximum of inter-story drift ratio ($\theta_{IDR,m}$) was ranged 0.5 to1.97% and 0.54 to 3.07% under far- and near-field records, respectively. Moreover, the maximum residual IDR ($\theta_{Res\cdot IDR}$) of the archetypes were negligible indicated the rocking system could prevent permanent damage. As a result, the designed archetypes satisfied the design limit of 2 and 0.5% *IDR* and residual *IDR*, respectively.

• It was observed that net IDRs ($\theta_{net.IDR}$) ranged 0.05-0.71% and 0.05-0.43% under far- and near-field records, respectively. As a result, most of the displacement resulted from the rigid rocking motion of the archetypes, which directly decreased the structural damage because of their rocking feature.

• Although higher $\theta_{IDR}$ emerged in archetypes under NF-pulse earthquakes than far-field ones, less $\theta_{net.IDR}$ occurred, which resulted in their uniform displacement distribution over the height of archetypes. Therefore, damage probability of structural elements and drift-sensitive components could be lower during the NF-pulse earthquake.

• It was found from the mean values of intensity index $I_s$ as the ratio of $\theta_{EDP}$ under *MCE* to *DBE* level that $\theta_{EDP}$ of archetypes for all the considered *EDPs* at *MCE* intensity was higher than that of the *DBE* level; but, the increasing rate of $\theta_{net.IDR}$ and $\theta_{roof\text{-}acc}$ values were lower than $\theta_{IDR}$. Moreover, the influence of seismic risk level on $\theta_{EDP}$ of archetypes under far-field earthquakes was more than the near-field ones. The values of earthquake type $I_{eq}$ index as the ratio of $\theta_{EDP}$ of archetypes under *NF*-pulse to far-field records indicated that the responses of all *EDPs*, except net *IDRs*, resulting near-fault earthquakes were higher than those of the far-field ones due to the pulse effect of near-field earthquakes.

• It was found that all the $\theta_{EDP}$ except $\theta_{IDR}$ of archetypes were increased by increasing the height archetypes. $\theta_{IDR}$ of taller archetypes was decreased due to their higher flexibility than that of shorter archetypes. Also, the damage probability of space archetypes due to their higher $\theta_{net.IDR}$ and $\theta_{acc}$ values were less than that of perimeter archetypes. As a result, the damage probability of rigid components and acceleration-sensitive non-structural components of archetypes under far-field records was higher than that of the NF-pulse ones due to their higher floor acceleration ($\theta_{acc}$). Moreover, it was shown that $\theta_{EDP}$ for the archetypes located at high seismicity (*SDC* $D_{\max}$) was higher than the lower one (*SDC* $D_{\min}$).

## References


Ajrab, J.J., Pekcan, G. and Mander, J.B. (2004), "Rocking wall-frame structures with supplemental tendon systems", *J. Struct. Eng.*, **130**(6), 895-903.

ASCE (2010), Minimum Design Loads for Buildings and Other Structures, *ASCE Standard ASCE/SEI 7-05*, American Society of Civil Engineers, Reston, Virginia.

ATC (2004), *Engineering demand parameters for non-structural components, Report No. ATC-58*, Applied Technology Council, Redwood City, CA.

Eatherton, M.R. and Hajjar, J.F. (2010), "Large-scale cyclic and hybrid simulation testing and development of a controlled-rocking steel building system with replaceable fuses", Ph.D. Dissertation, Illinois at Urbana-Champaign University, Champaign, IL.

Eatherton, M.R., Ma, X., Krawinkler, H., Mar, D., Billington, S., Hajjar, J.F. and Deierlein, G.G. (2014), "Design concepts for controlled rocking of self-centering steel-braced frames", *J. Struct. Eng.*, **140**(11), 195-203.

Francesco, S., Palermo, A. and Pampanin, S. (2015), "Quasi-static cyclic testing of two-thirds scale unbonded posttensioned rocking dissipative timber walls", *J. Struct. Eng.*, **142**(4), E4015005.

FEMA (2009), *Quantification of Building Seismic Performance Factors, Report No. FEMA P695*, Federal Emergency Management Agency, Washington, DC.

Grigorian, C. and Grigorian, M. (2015), "Performance control and efficient design of rocking-wall moment frames", *J. Struct. Eng.*, **142**(2), 04015139.

Gupta, A. and Krawinkler, H. (1999), "Seismic demands for the performance evaluation of steel moment resisting frame structures", Ph.D. Dissertation, Stanford University, Stanford, California.

Hall, K.S., Eatherton, M. and Hajjar, J.F. (2010), "Nonlinear behavior of controlled rocking steel-framed building systems with replaceable energy dissipating fuses", Rep. No. NSEL-026, Newmark Structural Engineering Laboratory Report Series, Urbana, IL.

Housner, G.W. (1963), "The behavior of inverted pendulum structures during earthquakes", *Bull. Seism. Soc. Am.*, **53**(2), 403-417.

IBC, I. (2006), *International building code*, International Code Council, Inc. (formerly BOCA, ICBO and SBCCI), 4051, 60478-65795.

ITG ACI (2009), *Requirements for Design of a Special Unbonded Post-Tensioned Precast Shear Wall, Report No. ACI ITG-5.2-09*, American Concrete Institute, Farmington Hills, MI.

Iwashita, K., Kimura, H., Kasuga, Y. and Suzuki, N. (2002), "Shaking table test of a steel frame allowing uplift", *J. Struct. Constr. Eng.*, **1**(561), 47-54.

Ma, X., Borchers, E., Pena, A., Krawinkler, H. and Deierlein, G. (2010), "Design and behavior of steel shear plates with openings as energy-dissipating fuses", Report, No. 173, John A. Blume Earthquake Engineering Center Technical, USA.

Ma, X. (2011), "Seismic design and behavior of self-centering braced frame with and energy-dissipating fuses", Ph.D. Dissertation, Stanford University, Stanford, USA.

OpenSees (2011), *Open System for Earthquake Engineering Simulation*, Pacific Earthquake Engineering research Center, University of California.

Rahgozar, N., Moghadam, A.S., Rahgozar, N. and Aziminejad, A. (2016), "Performance evaluation of self-centring steel-braced frame", *Proc. Inst. Civ. Eng. Struct. Build.*, 1-14, doi: 10.1680/jstbu.15.00136.

Rahgozar, N., Moghadam, A.S., Rahgozar, N. and Aziminejad, A. (2016), "Inelastic displacement ratios of fully self-centering controlled rocking systems subjected to near-source pulse-like ground motions", *Eng. Struct.*, **108**(1), 113-133.

Rahgozar, N., Moghadam, A.S. and Aziminejad, A. (2016), "Quantification of seismic performance factors for self-centering controlled rocking special concentrically braced frame", *Struct. Des. Tall Spec. Build.*, **25**(14), 700-723.

Roke, D., Sause, R., Ricles, J.M., Seo, C. and Lee, K. (2006), "Self-centering seismic-resistant steel concentrically-braced frames", *Proceedings of the 8th US National Conference on Earthquake Engineering, EERI, San Francisco, April*, 18-22.

Somerville, P.G., Smith, N.F., Graves, R.W. and Abrahamson, N.A. (1997), "Modification of empirical strong ground motion attenuation relations to include the amplitude and duration effects of rupture directivity", *Seismol. Res. Lett.*, **68**(1), 199-222.

Toranzo, L.A., Restrepo, J.I., Mander, J.B. and Carr, A.J. (2009), "Shake-table tests of confined-masonry rocking walls with supplementary hysteretic damping", *J. Earthq. Eng.*, **13**(6), 882-898.

Uriz, P. and Mahin, S.A. (2004), "Seismic vulnerability assessment of concentrically braced steel frames", *Int. J. Steel Struct.*, **4**(4), 239-248.

Walsh, K.Q. and Kurama, Y.C. (2012), "Effects of loading conditions on the behavior of unbounded post-tensioning strand-anchorage systems", *PCI J.*, **57**(1), 76-96.


*CC*